Contents lists available at ScienceDirect

Journal of Colloid and Interface Science
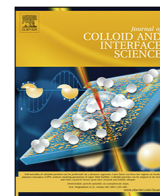
Oxygen vacancy-rich *N*-doped carbon encapsulated BiOCl-CNTs heterostructures as robust electrocatalyst synergistically promote oxygen reduction and Zn-air batteries

Xue Shao [a], Yuting Yang [a], Yi Liu [a], Puxuan Yan [a], Shuqing Zhou [a], Tayirjan Taylor Isimjan [b,*], Xiulin Yang [a,*]

[a] Guangxi Key Laboratory of Low Carbon Energy Materials, School of Chemistry and Pharmaceutical Sciences, Guangxi Normal University, Guilin 541004, China
[b] Saudi Arabia Basic Industries Corporation (SABIC) at King Abdullah University of Science and Technology (KAUST), Thuwal 23955-6900, Saudi Arabia

GRAPHICAL ABSTRACT

An oxygen vacancy-rich *N*-doped carbon encapsulated BiOCl-CNTs catalyst is constructed by stepwise hydrothermal reaction, carbonization and etching conversion methods. The designed catalyst exhibits excellent electrocatalytic activity and stability in oxygen reduction reaction and zinc-air battery applications.
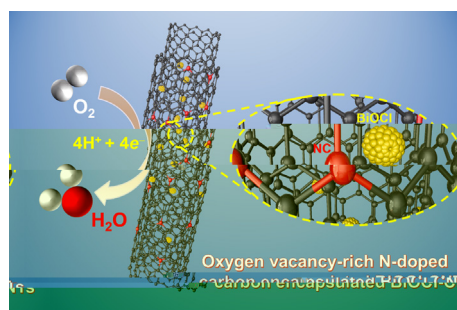
ARTICLE INFO

ABSTRACT

The development of non-precious metal catalysts for oxygen reduction reactions (ORR) is vital for promising clean energy technologies such as fuel cells, and zinc-air batteries. Herein, we present a stepwise synthesis of *N*-doped and carbon encapsulated BiOCl-CNTs heterostructures. Electrocatalytic ORR studies show that the optimized catalyst has a high half-wave potential ($E_{1/2}$) of 0.85 V (vs. RHE), large limiting current density (-5.34 mA cm^{-2}@0.6 V) in alkaline medium, and nearly perfect $4e^-$ reduction characteristics, even surpassing commercial Pt/C. Meanwhile, the catalyst has exceptional durability (above 97.5 % after 40000 s) and strong resistance towards methanol poisoning. The good ORR activity also results in high-performance zinc-air batteries with a specific capacity (724 mAh g^{-1}@10 mA cm^{-2}), a high open-circuit potential of 1.51 V and a peak power density of 170.7 mW cm^{-2}, as well as an ultra-long charge–discharge cycle stability (155 h), comparable with the Pt/C catalyst. The catalytic mechanism reveals that the excellent electrocatalytic performance originates from the synergistic effect of N doping, oxygen vacancies, and BiOCl sites.

© 2021 Elsevier Inc. All rights reserved.

1. Introduction

The massive energy consumption triggering a fossil-fuel-based energy crisis leads to an increasing interest in renewable clean

* Corresponding authors.
  E-mail addresses: isimjant@sabic.com (T. Taylor Isimjan), xlyang@gxnu.edu.cn (X. Yang).

energy storage and conversion systems [1]. Among the various energy conversion devices, the Zn-air battery has attracted considerable attention because of its safety, high energy density, and commercial viability [2,3]. Zn-air batteries are made of cheap materials (Zn, KOH and carbon) with a high theoretical energy density of 1084 Wh kg^{-1} [4]. Moreover, they are safe and easy to recycle. The Zn resource in the earth is 300 times higher than that of Li. Therefore, it does not pose any threat of resource limitation even if all the cars in the entire world are power by Zn-air batteries. Most

are uniformly ground and transferred to a ceramic container. Finally, the NC@Bi-CNTs was carbonized at 950 °C in argon for 2 h with a heating rate of 5 °C min^{-1}. The samples obtained are denoted according to their annealing temperature as NC@Bi-CNTs-900, −950 and −1000, respectively.

As a control, NC@Bi and N-CNTs were also prepared at 950 °C by the similar method described above, where PDA@Bi and CNTs were used instead of PDA@Bi-CNTs, respectively. In addition, C@Bi-CNTs (without adding melamine) was synthesized by a similar method.

2.5. P e a q i   f NC@BiOC -CNT

The NC@Bi-CNTs was further immersed in aqua regia (HNO$_3$/HCl = 1/3) for 12 h, and rinsed with abundant DI-water to be neutral. The resulted product was named as NC@BiOCl-CNTs. As a control, NC@BiOCl and C@BiOCl-CNTs were synthesized by a similar method, with NC@Bi and C@Bi-CNTs as the precursors, respectively.

2.6. Cha ac e i q i

Scanning electron microscope (SEM) (FEI Quanta 200 FEG) and transmission electron microscope (TEM) (TF20, JEOL 2100F) with elemental mapping were used to characterize the morphology and microscopic structure of the catalyst. X-ray powder diffraction (XRD, Rigaku, D/ Max-3C, Japan, scanning rate: 5° min^{-1}) and confocal Raman spectroscopy (Renishaw, England) were used to characterize the crystal structure of the samples. The chemical states of the catalyst were analyzed by X-ray photoelectron spectroscopy (XPS, ESCALAB 250Xi). Brunauer–Emmett–Teller (BET) and -Plot methods were used to measure the specific surface area and pore size distribution, respectively. Elemental composition of the samples was determined by inductively coupled plasma-atomic emission spectrometry (ICP-AES). The nitrogen content in the catalytic material was measured and analyzed using an elemental analyzer (PE2400 II).

2.7. E ec de fab ica i

In this work, the rotating ring disk electrode (RRDE, disk area = 0.247 cm^2) was polished and selected as the working electrode. For the preparation of catalyst ink: 4 mg black powder was weighed and dispersed into 1 mL 5 wt% Nafion solution (the volume ratio of isopropanol/water = 1/3). Catalyst ink droplets of 19.6 μL were added to the surface of the polished RRDE with a pipette-gun and dried in a natural environment. The catalyst loading and Pt/C loading on the working electrode were 0.318 and 0.081 mg cm^{-2}, respectively.

The electrocatalytic ORR performance is obtained by rotating ring-disk electrodes in a three-electrode system, while the performance of the zinc-air battery is achieved by a home-made zinc-air battery device (see supporting information for details). Each measurement was repeated at least three times to ensure the reproducibility of the results.

3. Results and discussion

3.1. S he i a d c a i a a i

The NC@BiOCl-CNTs hybrid material is constructed through a controllable four-step process, which involves Bi NPs reduction on CNT surface, PDA packaging, nitrogen doping, and BiOCl formation by aqua regia etching (Fig. 1a). In the first step, BDC-NH$_2$ is used as a reducing agent, and PVP is used as a modifier to reduce Bi NPs on CNT surface at high temperature to form Bi-CNTs

(Fig. 1b). XRD pattern shows that the Bi NPs matches the hexagonal-close-packed (hcp) metallic Bi (JCPDS: 44–1246) [30]. Second, the dopamine monomer polymerizes at high temperatures and wraps on the Bi-CNT surface to form PDA@Bi-CNTs [31]. Third, PDA@Bi-CNTs are carbonized at 950 °C, and melamine is used as a nitrogen source to form NC@Bi-CNTs (Fig. 1c and Fig. S2). Finally, after etching with aqua regia, most of the bare Bi NPs dissolve into the solution, and a small portion of the Bi NPs meshed by the carbon grid is transformed into BiOCl species, thereby obtaining NC@BiOCl-CNTs hybrid material (Fig. 1d). The clear four distinct characteristic peaks at 11.98°, 25.86°, 32.50°, and 33.45° are ascribed to the (001), (101), (110) and (102) crystal planes of BiOCl (JCPDS: 06–0249). Notably, when the hybrid material is subjected to continuous 20 cycles of CV treatment (0.05–1.15 V vs. RHE) (Fig. S3), the crystal structure of BiOCl does not change, implying that it has good ORR stability. Besides, three additional diffraction peaks appeared at 14.84°, 16.67°, and 22.77° after electrochemical treatment are corresponding to the hexagonal carbon (110), (002), and (120) crystal faces.

3.2. Mic   G e a d   i a a i

Scanning electron microscopy (SEM) and transmission electron microscopy (TEM) were used to investigate the morphologies and microstructures of NC@Bi-CNTs and NC@BiOCl-CNTs. The surface of CNTs in NC@Bi-CNTs is decorated with dense particulate maters (Fig. 2a). After etching with aqua regia, the NC@BiOCl-CNTs surface becomes relatively smooth, due to the gradual dissolution of the Bi particles (Fig. 2b). The TEM image shows that some particulate materials are randomly distributed on the CNTs surface (Fig. 2c). The high-resolution TEM images demonstrate that a set of clear lattice fringes of 0.34 nm is typical C (002) crystal faces. The lattice spacing of 0.27 nm belongs to the (102) crystal faces of BiOCl (Fig. 2d-e) [32], respectively. The selected area diffraction pattern (SAED) shows two sets of relatively distinctive diffraction rings index the (101) and (102) crystal planes of BiOCl that confirm the tetragonal structure (Fig. 2f). In addition, HAADF-STEM and corresponding element mappings appear that Bi, Cl, C, N, and O elements are uniformly distributed on the surface of NC@BiOCl-CNTs (Fig. 2g). The metal content of Bi in NC@BiOCl-CNTs was measured by ICP-AES (Table S1), and the result showed that the weight percentage of Bi was about 2.35 wt%.

Raman spectroscopy is an effective method to analyze the defect structure and graphitization degree of carbon materials. Generally, the intensity ratio of D-band ($_3$ carbon) and graphitic G-band ($_2$ carbon) (I_D/I_G) is used to evaluate the index of carbon disorders [33]. As shown in Fig. 3a, the NC@BiOCl-CNTs synthesized at 950 °C has the smallest I_D/I_G value (0.85) relative to the samples prepared at 900 °C (0.91) and 1000 °C (0.93), indicating that the samples prepared at 950 °C have higher graphitization degree and conductivity, thus facilitating electron transfer in the electrochemical ORR process [34]. Compared with C@BiOCl-CNTs (0.87) and NC@BiOCl (0.96), the doping of N element has little effect on the graphitization of hybrid materials, while the introduction of CNTs can greatly enhance the graphitization and conductivity of hybrid materials (Fig. 3b). Studies have shown that the graphitization degree of carbon and suitable N species contribute to ORR activity [35,36]. Table S2 summarizes the elemental analysis results of different materials, indicating that the NC@BiOCl-CNTs catalyst has the highest N content (1.98 wt%). According to previous reports, the N-doped component is chemically active that increases the more active sites, and changes the electronegativity of the adjacent C atom, thus enhancing the ORR intrinsic activity [37]. Moreover, BET measurement and related porosity analysis showed that NC@BiOCl-CNTs had a large specific surface area of
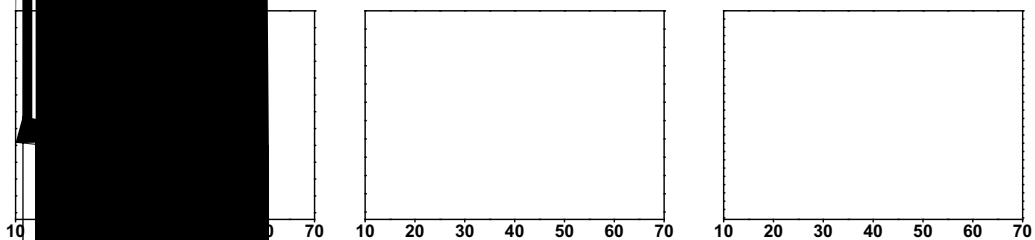
357.5 m^2 g^{-1} with a   er of 7.8 nm (inset)
(Fig. 3c), indicating a   feature. This meso-
porous feature with a   rea can expose more
active sites, and help   as emission, thereby
improving the ORR ca

3.3. Che ica   a e a a i

The chemical valence states and bonding configurations of the
synthesized catalysts were further studied by X-ray photoelectron
spectroscopy (XPS). As displayed in Fig. S4a, NC@BiOCl-CNTs
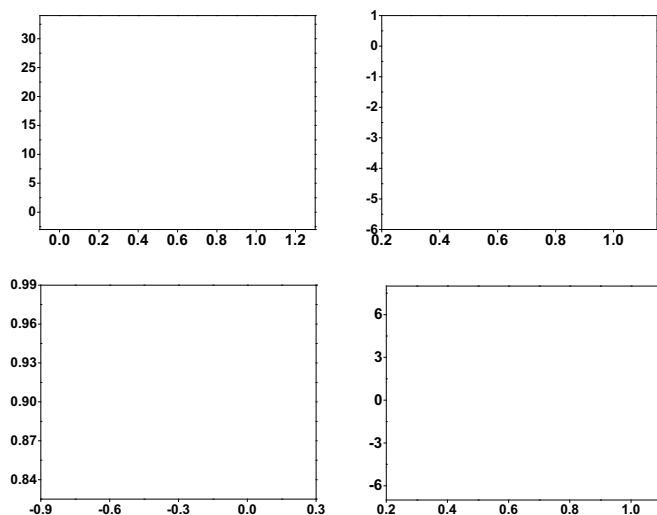
itly stated, the catalysts discussed below are prepared by calcination at 950 °C.

The catalyst activity of NC@BiOCl-CNTs and the comparative catalyst in N_2– or O_2-saturated alkaline solution was first investigated by cyclic voltammetry (CV) at a constant scan rate of 50 mV s^{-1} (Fig. 5a). Notably, no strong cyclic voltammetry response was observed in the N_2-saturation KOH electrolyte, whereas the NC@BiOCl-CNTs catalyst had a significant cathodic reduction peak (pacing potential 0.87 V vs. RHE) in the case of O_2-saturated, higher than the characteristic peak values of C@BiOCl-CNTs and NC@BiOCl catalysts. Subsequently, a similar tendency was detected on the linear sweep voltammeter (LSV) curves (Fig. 5b). The $E_{1/2}$ value of NC@BiOCl-CNTs (0.85 V) differs by 0.1 V from the state-of-the-art noble metal Pt/C catalyst (0.86 V). In particular, the limiting current density of the NC@BiOCl-CNTs catalyst is 5.34 mA cm^{-2} at 0.6 V, which is approximately 1.08-fold higher than that of commercial Pt/C (4.96 mA cm^{-2}). Meanwhile, the NC@BiOCl-CNTs also exhibits significantly superior ORR activity than the *N*-free C@BiOCl-CNTs, CNTs-free NC@BiOCl, and BiOCl-free *N*-CNTs (Table S3) and is comparable to most non-noble metal ORR electrocatalysts reported so far (Table S4). Notably, when NC@Bi-CNTs was converted to NC@BiOCl-CNTs by immersion in aqua regia, the current density rapidly increased from 4 mA cm^{-2} to 5.34 mA cm^{-2} at 0.6 V, directly indicating that the BiOCl sites enhanced the overall performance of the NC@BiOCl-CNTs catalyst (Fig. S7).

The electron transfer number and H_2O_2 yield of NC@BiOCl-CNTs catalyst were obtained using the RRDE method (Fig. 5c). The results reveal that the H_2O_2 yield is less than 20 % in the potential range of 0.2 to 0.8 V, which is indirect evidence of the four-electron selectivity of the ORR process. Moreover, the NC@BiOCl-CNTs show a Tafel slope of 68.7 mV dec^{-1} (Fig. 5d), which is much lower than C@BiOCl-CNTs (76.2 mV dec^{-1}), NC@BiOCl (85.2 mV dec^{-1}), and *N*-CNTs (72.1 mV dec^{-1}), verifying fast reaction kinetics [14].

Besides, the LSV measurements (400 to 2025 rpm) at different speeds were also performed (Fig. 5e) [51]. The average electron transfer number was calculated to be 4 from the Koutecky-Levich (K–L) diagram according to the LSV curve in the voltage range of 0.3–0.7 V (inset in Fig. 5e) [52]. The percentage of H_2O_2 and the number of electrons transferred by the catalyst at different potentials are calculated (Fig. 5f). The result is in agreement with that of

the K-L curve. In addition, the charge transfer resistance (R_{ct}) of the highly active NC@BiOCl-CNTs catalyst was lower than those of all control catalysts, as measured by electrochemical impedance spectroscopy (EIS) (Fig. S8), implying a faster electron transfer rate and higher conductivity [53].

The electrochemical double-layer capacitance (C_{dl}) of an electrocatalyst is commonly used to determine its electrochemically active surface area (ECSA) using the polarization curves. The C_{dl} is obtained at different scan rates in the non-Faraday region (Fig. 6a, Figs. S9a-b) [13]. In general, the slope relationship between capacitance current density and scanning rate can be used as a parameter for ECSA demonstration. As depicted in Fig. 6b, the Cdl of NC@BiOCl-CNTs catalyst was 16.89 mF cm^{-2}, which was 1.2 and 6.3 times higher than those of C@BiOCl-CNTs (13.62 mF cm^{-2}) and NC@BiOCl (2.7 mF cm^{-2}), respectively, evidencing that NC@BiOCl-CNTs catalyst has a larger ECSA, thereby exposing more accessible active sites [54]. Fig. 6c and Figs. S9c-d shows the linear relationship between the oxidation peak and the scanning rate of the catalyst in KCl solution containing $K_3(Fe(CN)_6)$. According to the Randles-Sevcik equation (Fig. 6d) [23], the ECSA of NC@BiOCl-CNTs was 0.71 m^2 g^{-1}, and 1.4 and 1.5 times higher than those of C@BiOCl-CNTs (0.48 m^2 g^{-1}) and NC@BiOCl (0.46 m^2 g^{-1}). This observation is inconsistent with the C_{dl} results.

The methanol crossover tolerance performance of NC@BiOCl-CNTs is investigated by the chronoamperometry (CA) method. Fig. 7a shows that NC@BiOCl-CNTs reveals excellent tolerance to the methanol crossover effect, while the current density of Pt/C drops sharply after injecting methanol into the solution at ca. 200 s. Moreover, the NC@BiOCl-CNTs exhibit long-lasting stability and the current-loss of only 2.5% after 40000 s of operation. On the other hand, the Pt/C current-loss is much greater, about 12.6% (Fig. 7b) under the same conditions [55]. In addition, it is noteworthy that after 2000 CV cycles in succession, the limiting current density of NC@BiOCl-CNTs was slightly decreased by 0.17 mA cm^{-2}, while the limiting current density of Pt/C was significantly decreased by 1.51 mA cm^{-2} (Fig. S10), further reflecting its excellent stability. To study the active sites of highly efficient catalysts, SCN^- was introduced as the masking agent [56]. Fig. 7c shows that the limiting current density and $E_{1/2}$ of NC@BiOCl-CNTs both decrease markedly after the addition of 0.01 M SCN^-. This result indicates that SCN^- binding agents can coordinate with Bi species
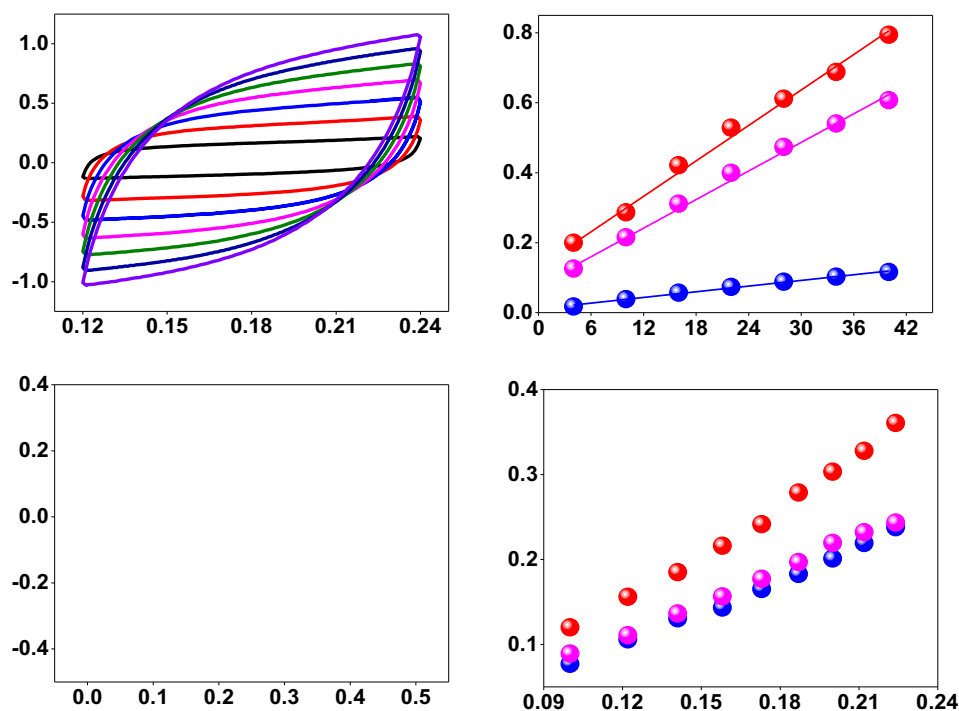
to form a stable coordination compound, which decreases the ORR performance of the catalyst [2,57].

3.5. Zinc-air battery made

Finally, a zinc-air battery with NC@BiOCl-CNTs as the air–cathode was constructed to explore the practical application of energy devices, as displayed in Fig. 8a. The NC@BiOCl-CNTs-based and benchmark Pt/C-based battery exhibits a platform voltage of 1.25 and 1.17 V (Fig. 8b). Also, the NC@BiOCl-CNTs-based system delivers the specific capacities of 724 mAh g^{-1} at a discharge current density of 10 mA cm^{-2}, outperforming the battery assembled by Pt-based catalyst [58]. The discharge voltage and power density are presented in Fig. 8c, NC@BiOCl-CNTs battery provides a power density of 170.7 mW cm^{-2}, far exceeding that of Pt/C (129.6 mW cm^{-2}) and most pre-viously reported systems (Table S5). NC@BiOCl-CNTs catalyst affords a stable open-circuit voltage of about 1.51 V in comparison with that of the commercial Pt/C (Fig. 8d). Likewise, the NC@BiOCl-CNTs battery in series can illuminate the red light-emitting diode (LED) with the required 3.0 V voltage (Fig. 8e). As shown in Fig. 8f, NC@BiOCl-CNTs catalyst maintains a relatively stable discharge capacity at different current densities. Notable, the platform voltage was also restored to 1.27 V when the discharge current density was restored to 2 mA cm^{-2}, indicating good reversibility based on the rechargeable zinc-air battery. In Fig. 8g-h, the stability of NC@BiOCl-CNTs is also evaluated by cyclic durabil-ity and rechargeability. After 155 h of long-term operation, the NC@BiOCl-CNTs-based battery does not show any evidence of volt-age drop, exhibiting excellent cycle stability compared to the com-mercial Pt/C. The high potential for NC@BiOCl-CNTs as an
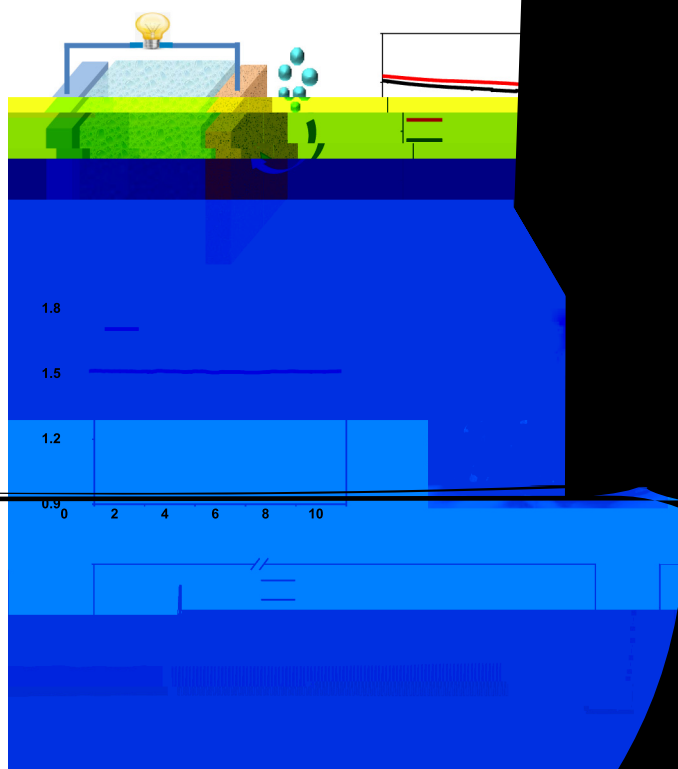
electrocatalyst for oxygen reduction is further demonstrated by a comprehensive comparison with noble metal Pt/C catalyst, making it more competitive in practical applications.

4. Conclusion

In summary, nanostructured NC-meshed BiOCl parti
successfully prepared via a feasible strategy for the fir
doped carbon encapsulation on metal nanocatalys
ensures high conductivity but also prevents the cata
tion. The NC@BiOCl-CNTs catalyst displayed excellen
compared with commercial Pt/C in 0.1 M KOH
importantly, the NC@BiOCl-CNTs catalyst coupled
and relatively short diffusion lengths. In addition, t
ies using NC@BiOCl-CNTs catalyst as an air catho
competitive peak power density (170.7 mW cm
stably for>155 h at 10 mA cm^{-2}. This work may
for the rational design of highly active ORR ele

CRediT authorship contribution statement

Xue Shao: Investigation, Methodology. Yut
tion, Data curation. Yi Liu: Data curation. Pux
ogy. Shuqing Zhou: Data curation. Tayirj
Writing–review & editing. : . Xiulin Yang: Sup
view & editing.

Declaration of Competing Interest

The authors declare that they have no kno
cial interests or personal relationships that
to influence the work reported in this paper.

[7] H. Yang, L. Gong, H. Wang, C. Dong, J. Wang, K. Qi, H. Liu, X. Guo, B.Y. Xia, Preparation of nickel-iron hydroxides by microorganism corrosion for efficient oxygen evolution, Nat. Commun. 11 (2020) 5075.

[8] T. Wang, Y. He, Y. Liu, F. Guo, X. Li, H. Chen, H. Li, Z. Lin, A ZIF-triggered rapid polymerization of dopamine renders Co/N-codoped cage-in-cage porous carbon for highly efficient oxygen reduction and evolution, Nano Energy 79 (2021) 105487.

[9] G. Liu, J. Li, J. Fu, G. Jiang, G. Lui, D. Luo, Y.P. Deng, J. Zhang, Z.P. Cano, A. Yu, D. Su, Z. Bai, L. Yang, Z. Chen, An Oxygen-Vacancy-Rich Semiconductor-Supported Bifunctional Catalyst for Efficient and Stable Zinc-Air Batteries, Adv. Mater. 31 (2019) 1806761.

[10] Z. Liang, H.Y. Wang, H. Zheng, W. Zhang, R. Cao, Porphyrin-based frameworks for oxygen electrocatalysis and catalytic reduction of carbon dioxide, Chem. Soc. Rev. 50 (2021) 2540–2581.

[11] M. Luo, W. Sun, B.B. Xu, H. Pan, Y. Jiang, Interface Engineering of Air Electrocatalysts for Rechargeable Zinc-Air Batteries, Adv. Energy Mater. 11 (2020) 2002762.

[12] T. Tang, W.J. Jiang, X.Z. Liu, J. Deng, S. Niu, B. Wang, S.F. Jin, Q. Zhang, L. Gu, J.S. Hu, L.J. Wan, Metastable Rock Salt Oxide-Mediated Synthesis of High-Density Dual-Protected M@NC for Long-Life Rechargeable Zinc-Air Batteries with Record Power Density, J. Am. Chem. Soc. 142 (2020) 7116–7127.

[13] R. Zhao, Q. Li, Z. Chen, V. Jose, X. Jiang, G. Fu, J.-M. Lee, S. Huang, B, N-doped ultrathin carbon nanosheet superstructure for high-performance oxygen reduction reaction in rechargeable zinc-air battery, Carbon 164 (2020) 398–406.

[14] Y. Wang, N. Xu, R. He, L. Peng, D. Cai, J. Qiao, Large-scale defect-engineering tailored tri-doped graphene as a metal-free bifunctional catalyst for superior electrocatalytic oxygen reaction in rechargeable Zn-air battery, Appl. Catal. B: Environ. 285 (2021) 119811.

[15] S. Huang, Y. Meng, Y. Cao, S. He, X. Li, S. Tong, M. Wu, N⁻, O⁻ and P-doped hollow carbons: Metal-free bifunctional electrocatalysts for hydrogen evolution and oxygen reduction reactions, Appl. Catal. B: Environ. 248 (2019) 239–248.

[16] J. Qin, Z. Liu, D. Wu, J. Yang, Optimizing the electronic structure of cobalt via synergized oxygen vacancy and Co-N-C to boost reversible oxygen electrocatalysis for rechargeable Zn-air batteries, Appl. Catal. B: Environ. 278 (2020) 119300.

[17] L. Huang, S. Zaman, X. Tian, Z. Wang, W. Fang, B.Y. Xia, Advanced Platinum-Based Oxygen Reduction Electrocatalysts for Fuel Cells, Acc. Chem. Res. 54 (2021) 311–322.

[18] D. Chen, J. Zhu, X. Mu, R. Cheng, W. Li, S. Liu, Z. Pu, C. Lin, S. Mu, Nitrogen-Doped carbon coupled FeNi₃ intermetallic compound as advanced bifunctional electrocatalyst for OER, ORR and zn-air batteries, Appl. Catal. B: Environ. 268 (2020) 118729.

[19] Q. Lu, J. Yu, X. Zou, K. Liao, P. Tan, W. Zhou, M. Ni, Z. Shao, Self-Catalyzed Growth of Co, N-Codoped CNTs on Carbon-Encased CoSx Surface: A Noble-Metal-Free Bifunctional Oxygen Electrocatalyst for Flexible Solid Zn-Air Batteries, Adv. Funct. Mater. 29 (2019) 1904481.

[20] C. Tang, H.F. Wang, Q. Zhang, Multiscale Principles To Boost Reactivity in Gas-Involving Energy Electrocatalysis, Acc. Chem. Res. 51 (2018) 881–889.

[21] D. Alba-Molina, A.R. Puente Santiago, J.J. Giner-Casares, E. Rodríguez-Castellón, M.T. Martín-Romero, L. Camacho, R. Luque, M. Cano, Correction: Tailoring the ORR and HER electrocatalytic performances of gold nanoparticles through metal–ligand interfaces, J. Mater. Chem. A 7 (2019) 20435.

[22] L. Yan, Z. Xu, W. Hu, J. Ning, Y. Zhong, Y. Hu, Formation of sandwiched leaf-like CNTs-Co/ZnCo₂O₄@NC-CNTs nanohybrids for high-power-density rechargeable Zn-air batteries, Nano Energy 82 (2021) 105710.

[23] M. Qian, M. Xu, S. Zhou, J. Tian, T. Taylor Isimjan, Z. Shi, X. Yang, Template synthesis of two-dimensional ternary nickel-cobalt-nitrogen co-doped porous carbon film: Promoting the conductivity and more active sites for oxygen reduction, J. Colloid Interface Sci. 564 (2020) 276–285.

[24] M.-A. Légaré, G. Bélanger-Chabot, R.D. Dewhurst, E. Welz, I. Krummenacher, B. Engels, H. Braunschweig, Nitrogen fixation and reduction at boron, Science 359 (2018) 896–900.

[25] E. Zhang, T. Wang, K. Yu, J. Liu, W. Chen, A. Li, H. Rong, R. Lin, S. Ji, X. Zheng, Y. Wang, L. Zheng, C. Chen, D. Wang, J. Zhang, Y. Li, Bismuth Single Atoms Resulting from Transformation of Metal-Organic Frameworks and Their Use as Electrocatalysts for CO₂ Reduction, J. Am. Chem. Soc. 141 (2019) 16569–16573.

[26] W. Ouyang, F. Teng, X. Fang, High Performance BiOCl Nanosheets/TiO₂ Nanotube Arrays Heterojunction UV Photodetector: The Influences of Self-Induced Inner Electric Fields in the BiOCl Nanosheets, Adv. Funct. Mater. 28 (2018) 1707178.

[27] R. Kashfi-Sadabad, S. Yazdani, T.D. Huan, Z. Cai, M.T. Pettes, Role of Oxygen Vacancy Defects in the Electrocatalytic Activity of Substoichiometric Molybdenum Oxide, J. Phys. Chem. C 122 (2018) 18212–18222.

[28] M. Zorko, P. Farinazzo Bergamo Dias Martins, J.G. Connell, P.P. Lopes, N.M. Markovic, V.R. Stamenkovic, D. Strmcnik, Improved Rate for the Oxygen Reduction Reaction in a Sulfuric Acid Electrolyte using a Pt(111) Surface Modified with Melamine, ACS Appl. Mater. Interfaces 13 (2021) 3369–3376.

[29] L. Feng, T. Wang, H. Sun, M. Jiang, Y. Chen, Carbon Nitride Anchored on a Nitrogen-Doped Carbon Nanotube Surface for Enhanced Oxygen Reduction Reaction, ACS Appl. Mater. Interfaces 12 (2020) 56954–56962.

[30] H. Jiang, L. Wang, Y. Li, B. Gao, Y. Guo, C. Yan, M. Zhuo, H. Wang, S. Zhao, High-selectivity electrochemical CO₂ reduction to formate at low overpotential over Bi catalyst with hexagonal sheet structure, Appl. Surf. Sci. 541 (2021) 148577.

[31] X. Cheng, P. Yan, S. Liu, M. Qian, B. Wang, Z. Wan, J. Tian, X.-C. Shen, T.T. Isimjan, X. Yang, Well-dispersed iron oxide stabilized Fe-N₄ active sites in porous N-doped carbon spheres as alternative superior catalyst for oxygen reduction, Int. J. Hydrogen Energy 44 (2019) 12127–12137.

[32] M. Li, S. Yu, H. Huang, X. Li, Y. Feng, C. Wang, Y. Wang, T. Ma, L. Guo, Y. Zhang, Unprecedented Eighteen-Faceted BiOCl with a Ternary Facet Junction Boosting Cascade Charge Flow and Photo-redox, Angew. Chem. Int. Ed. 58 (2019) 9517–9521.

[33] X. Cheng, S. Dou, G. Qin, B. Wang, P. Yan, T.T. Isimjan, X. Yang, Rational design of highly selective nitrogen-doped Fe₂O₃-CNTs catalyst towards H₂O₂ generation in alkaline media, Int. J. Hydrogen Energy 45 (2020) 6128–6137.

[34] A. Gupta, S.R. Dhakate, P. Pal, A. Dey, P.K. Iyer, D.K. Singh, Effect of graphitization temperature on structure and electrical conductivity of poly-acrylonitrile based carbon fibers, Diamond Relat. Mater. 78 (2017) 31–38.

[35] J. Zhao, Y. Liu, X. Quan, S. Chen, H. Yu, H. Zhao, Nitrogen-doped carbon with a high degree of graphitization derived from biomass as high-performance electrocatalyst for oxygen reduction reaction, Appl. Surf. Sci. 396 (2017) 986–993.

[36] S. Gadipelli, T. Zhao, S.A. Shevlin, Z. Guo, Switching effective oxygen reduction and evolution performance by controlled graphitization of a cobalt–nitrogen–carbon framework system, Energy Environ. Sci. 9 (2016) 1661–1667.

[37] S. Chen, L. Zhao, J. Ma, Y. Wang, L. Dai, J. Zhang, Edge-doping modulation of N, P-codoped porous carbon spheres for high-performance rechargeable Zn-air batteries, Nano Energy 60 (2019) 536–544.

[38] S. Dou, S. Zhou, H. Huang, P. Yan, E. Shoko, T.T. Isimjan, X. Yang, Metal-Organic Framework (MOF)-Derived Electron-Transfer Enhanced Homogeneous PdO-Rich Co₃O₄ as a Highly Efficient Bifunctional Catalyst for Sodium Borohydride Hydrolysis and 4-Nitrophenol Reduction, Chem. Eur. J. 26 (2020) 16923–16931.

[39] S. Dou, W. Zhang, Y. Yang, S. Zhou, X. Rao, P. Yan, T.T. Isimjan, X. Yang, Shaggy-like Ru-clusters decorated core-shell metal-organic framework-derived CoOx@NPC as high-efficiency catalyst for NaBH₄ hydrolysis, Int. J. Hydrogen Energy 46 (2021) 7772–7781.

[40] R. Rameshbabu, R. Sandhiya, G. Pecchi, M. Sathish, Effective coupling of Cu (II) with BiOCl nanosheets for high performance electrochemical supercapacitor and enhanced photocatalytic applications, Appl. Surf. Sci. 521 (2020) 146362.

[41] S. Abednatanzi, P. Gohari Derakhshandeh, K. Leus, H. Vrielinck, F. Callens, J. Schmidt, A. Savateev, P. Van Der Voort, Metal-free activation of molecular oxygen by covalent triazine frameworks for selective aerobic oxidation, Sci. Adv. 6 (2020) 2310.

[42] M. Qian, X. Cheng, T. Sun, J. Tian, T.T. Isimjan, Z. Shi, X. Yang, Synergistic catalytic effect of N-doped carbon embedded with CoFe-rich CoFe₂O₄ clusters as highly efficient catalyst towards oxygen reduction, J. Alloys Compd. 819 (2020) 153015.

[43] X. Ning, Y. Li, J. Ming, Q. Wang, H. Wang, Y. Cao, F. Peng, Y. Yang, H. Yu, Electronic synergism of pyridinic- and graphitic-nitrogen on N-doped carbons for the oxygen reduction reaction, Chem. Sci. 10 (2019) 1589–1596.

[44] P. Yan, L. Sun, S. Yuan, Y. Liu, W. Cen, Y. Chen, The promotion effects of graphitic and pyridinic N combinational doping on graphene for ORR, Appl. Surf. Sci. 445 (2018) 398–403.

[45] T. Jia, J. Wu, Z. Ji, C. Peng, Q. Liu, M. Shi, J. Zhu, H. Wang, D. Liu, M. Zhou, Surface defect engineering of Fe-doped Bi₇O₉I₃ microflowers for ameliorating charge-carrier separation and molecular oxygen activation, Appl. Catal. B: Environ. 284 (2021) 119727.

[46] P. Yan, M. Huang, B. Wang, Z. Wan, M. Qian, H. Yan, T.T. Isimjan, J. Tian, X. Yang, Oxygen defect-rich double-layer hierarchical porous Co₃O₄ arrays as high-efficient oxygen evolution catalyst for overall water splitting, J. Energy Chem. 47 (2020) 299–306.

[47] C. Tomon, A. Krittayavathananon, S. Sarawutanukul, S. Duangdangchote, N. Phattharasupakun, K. Homlamai, M. Sawangphruk, Enhancing bifunctional electrocatalysts of hollow Co₃O₄ nanorods with oxygen vacancies towards ORR and OER for Li–O₂ batteries, Electrochim. Acta 367 (2021) 137490.

[48] M.-C. Tsai, T.-T. Nguyen, N.G. Akalework, C.-J. Pan, J. Rick, Y.-F. Liao, W.-N. Su, B.-J. Hwang, Interplay between Molybdenum Dopant and Oxygen Vacancies in a TiO₂ Support Enhances the Oxygen Reduction Reaction, ACS Catal. 6 (2016) 6551–6559.

[49] L. Yi, J. Chen, P. Shao, J. Huang, X. Peng, J. Li, G. Wang, C. Zhang, Z. Wen, Molten-Salt-Assisted Synthesis of Bismuth Nanosheets for Long-term Continuous Electrocatalytic Conversion of CO₂ to Formate, Angew. Chem. Int. Ed. 59 (2020) 20112–20119.

[50] J. Zhu, J. Fan, T. Cheng, M. Cao, Z. Sun, R. Zhou, L. Huang, D. Wang, Y. Li, Y. Wu, Bilayer nanosheets of unusual stoichiometric bismuth oxychloride for potassium ion storage and CO₂ reduction, Nano Energy 75 (2020) 104939.

[51] Z. Liang, X. Fan, H. Lei, J. Qi, Y. Li, J. Gao, M. Huo, H. Yuan, W. Zhang, H. Lin, H. Zheng, R. Cao, Cobalt-Nitrogen-Doped Helical Carbonaceous Nanotubes as a Class of Efficient Electrocatalysts for the Oxygen Reduction Reaction, Angew. Chem. Int. Ed. 57 (2018) 13187–13191.

[52] J. Lilloja, E. Kibena-Põldsepp, A. Sarapuu, M. Kodali, Y. Chen, T. Asset, M. Käärik, M. Merisalu, J. Paiste, J. Aruväli, A. Treshchalov, M. Rähn, J. Leis, V. Sammelselg, S. Holdcroft, P. Atanassov, K. Tammeveski, Cathode Catalysts Based on Cobalt- and Nitrogen-Doped Nanocarbon Composites for Anion Exchange Membrane Fuel Cells, ACS Appl. Energy Mater. 3 (2020) 5375–5384.

[53] B. Huang, X. Zhang, J. Cai, W. Liu, S. Lin, A novel MnO₂/rGO composite prepared by electrodeposition as a non-noble metal electrocatalyst for ORR, J. Appl. Electrochem. 49 (2019) 767–777.

[54] X.L. Wang, L.Z. Dong, M. Qiao, Y.J. Tang, J. Liu, Y. Li, S.L. Li, J.X. Su, Y.Q. Lan, Exploring the Performance Improvement of the Oxygen Evolution Reaction in a Stable Bimetal-Organic Framework System, Angew. Chem. Int. Ed. 57 (2018) 9660–9664.

[55] J. Wang, W. Zang, S. Xi, M. Kosari, S.J. Pennycook, H.C. Zeng, Trimetal atoms confined in openly accessible nitrogen-doped carbon constructs for an efficient ORR, J. Mater. Chem. A. 8 (2020) 17266–17275.

[56] Y. Cheng, J. Zhang, S.P. Jiang, Are metal-free pristine carbon nanotubes electrocatalytically active?, Chem Commun. 51 (2015) 13764–13767.

[57] Y. Wang, K. Qi, S. Yu, G. Jia, Z. Cheng, L. Zheng, Q. Wu, Q. Bao, Q. Wang, J. Zhao, X. Cui, W. Zheng, Revealing the Intrinsic Peroxidase-Like Catalytic Mechanism of Heterogeneous Single-Atom Co–MoS$_2$, Nano-Micro Lett. 11 (2019) 102.

[58] A. Kraytsberg, Y. Ein-Eli, The impact of nano-scaled materials on advanced metal–air battery systems, Nano Energy 2 (2013) 468–480.